Cell Reports
Physical Science

CellPress
OPEN ACCESS

Report

# Low-power continuous-wave all-optical magnetic switching in ferromagnetic nanoarrays

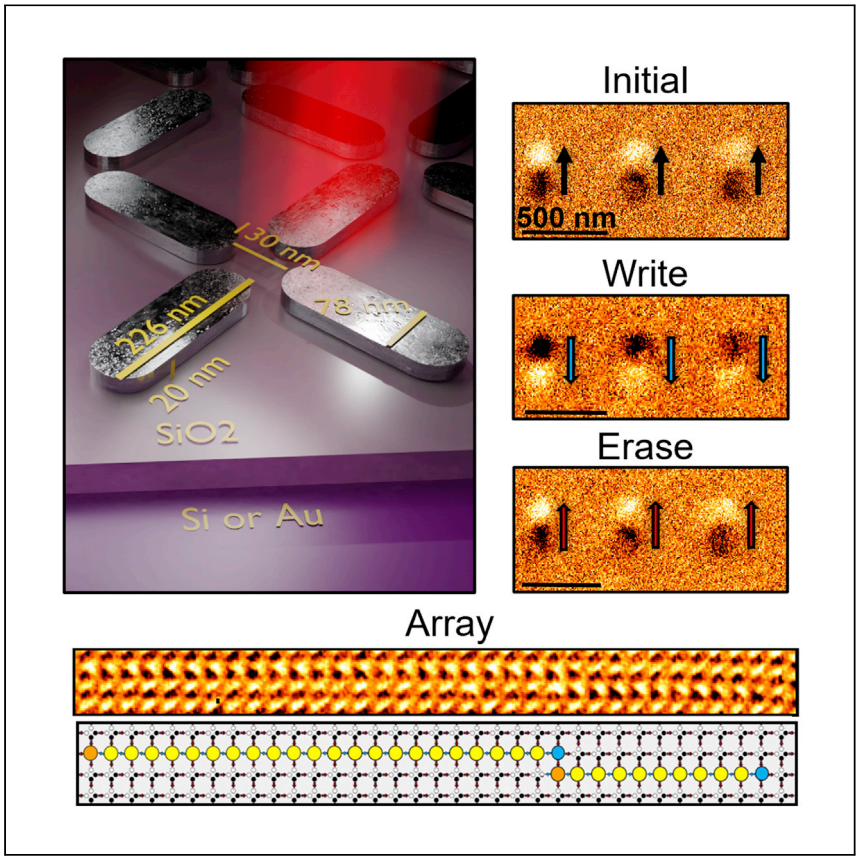


The power and material requirements of all-optical magnetic switching prevent technological integration. Stenning et al. develop a method of all-optical magnetic switching using a focused, low-power, linearly polarized laser and simple ferromagnetic materials. Enhanced asymmetric optical absorption allows deterministic switching of a broad range of nanomagnet dimensions at milliwatt powers.

Kilian D. Stenning, Xiaofei Xiao, Holly H. Holder, ..., Oscar W. Kennedy, Rupert F. Oulton, Will R. Branford

k.stenning18@imperial.ac.uk

## Highlights

AOMS often requires high-power lasers and rare materials

Ferromagnetic nanomagnets are switched with a low-power linearly polarized laser

Isolated and densely packed nanomagnets are written at powers as low as 2.74 mW

Asymmetry of light absorption provides the driving force for nanomagnet reversal

Stenning et al., Cell Reports Physical Science 4, 101291
March 15, 2023 
https://doi.org/10.1016/j.xcrp.2023.101291

Cell Reports
Physical Science

CellPress
OPEN ACCESS

Report

# Low-power continuous-wave all-optical magnetic switching in ferromagnetic nanoarrays

Kilian D. Stenning,[1,2,3,4,*] Xiaofei Xiao,[1,3] Holly H. Holder,[1] Jack C. Gartside,[1] Alex Vanstone,[1,2] Oscar W. Kennedy,[1,2] Rupert F. Oulton,[1] and Will R. Branford[1]

## SUMMARY

**All-optical magnetic switching promises ultrafast magnetization control without a magnetic field. Existing schemes typically require power-hungry femtosecond-pulsed lasers and complex magnetic materials. Here, we demonstrate deterministic, all-optical magnetic switching in simple ferromagnetic nanomagnets ($Ni_{81}Fe_{19}$, $Ni_{50}Fe_{50}$) with sub-diffraction limit dimensions using a focused low-power, linearly polarized continuous-wave laser. Isolated nanomagnets are switched across a range of dimensions, laser wavelengths, and powers. All square-geometry artificial spin ice vertex configurations are written at low powers (2.74 mW). Usually, switching with linearly polarized light is symmetry forbidden; here, the laser spot has a similar size to the nanomagnets, producing an absorption distribution that depends on the nanoisland-spot displacement. We attribute the deterministic switching to the transient dynamics of this asymmetric absorption. No switching is observed in Co or Ni nanostructures, suggesting the multi-species nature of NiFe plays a role. These results usher in inexpensive, low-power, optically controlled devices with impact across data storage, neuromorphic computation, and reconfigurable magnonics.**

## INTRODUCTION

Efficient optical control of magnetic materials is a long-standing goal for data storage and computational technologies. Continuous-wave exposure of magnetic materials can have a number of effects, from linearly polarized light-induced modifications of the magnetic anisotropy, susceptibility, and coercivity to magnetization control via angular momentum transfer from circularly polarized light.[1] The latter is promising for data storage, yet in ferromagnets, domains can only be grown (due to magnetic circular dichroism effects) and not switched. Of global data, 74% is stored magnetically and the predominant recording technology uses power-consuming magnetic fields with a plasmonically focused laser beam for heat-assisted magnetic recording.[2,3] Removing magnetic field requirements for all-optical magnetic switching (AOMS)[4–7] represents a next-generation class of local magnetization control, with intriguing switching effects beyond current thermodynamic descriptions and wide-ranging technological implications.

AOMS has been demonstrated in several schemes via ultrafast excitation with varying underlying switching mechanisms. Helicity-dependent switching with single or multiple femtosecond laser pulses has been observed in ferrimagnetic, ferromagnetic, and granular magnetic media.[4,8–12] In these systems, light serves to both demagnetize the material and realign the magnetization via angular momentum

[1]Blackett Laboratory, Imperial College London, London SW7 2AZ, UK

[2]London Centre for Nanotechnology, University College London, London WC1H 0AH, UK

[3]These authors contributed equally

[4]Lead contact

*Correspondence: k.stenning18@imperial.ac.uk

https://doi.org/10.1016/j.xcrp.2023.101291

transfer (arising from the inverse Faraday effect or magnetic circular dichroism). The effective field breaks system symmetry, driving magnetic reversal.

Helicity-independent switching (HIS) has been demonstrated with a single femtosecond pulse, yet is largely limited to rare earth ferrimagnets, typically GdFeCo.[8,13–19] In these systems, the electron and spin temperatures and the different band structures (with different demagnetization rates) between sublattices play a crucial role. As the system is excited, there is a marked increase in the electron and spin temperatures.[13] This leads to the FeCo sublattice rapidly demagnetizing within 1 ps, as observed in a number of ferromagnetic materials.[20] Because of the different magnetic moment, Gd demagnetizes at a slower rate, and partial angular momentum transfer to the demagnetizing FeCo results in a transient ferromagnetic state.[15] As the magnetization and temperatures equilibrate, the magnetization reverses. The same effect is observed with hot electron injection,[21] confirming the thermal nature of the theory. HIS has also been observed in rare earth-free ferrimagnets with near-identical sub-lattice demagnetization rates,[22] where switching is believed to be driven by exchange scattering and angular momentum transfer.

HIS in ferromagnets is typically observed when coupled to GdFeCo layers,[23–25] where spin-polarized currents generated from the HIS of GdFeCo transfer angular momentum to the demagnetized ferromagnetic layer, causing reversal.[25] HIS has been demonstrated in Pt/Co/Pt multilayers through a thermal process when focusing the laser spot to single-domain sizes,[26] implying that the boundary of the excitation plays an important role. These demonstrations have shown the promise of AOMS, but the requirement of huge femtosecond-pulsed megawatt lasers and exotic magnetic materials renders them unsuitable for device integration and upscaling for application. Additionally, the majority of studies concern continuous thin films or well-spaced single nanostructures,[17] restricting write density.

Artificial spin systems comprising networks of strongly interacting nanomagnets serve as promising hosts for future information-processing technologies, including nanomagnetic logic,[27,28] neuromorphic computation,[29–35] and reconfigurable magnonics.[36–43] Information can be stored in the magnetization of a single nanomagnet or the magnetic configuration of the entire network (microstate), where collective microstate-dependent dynamics[36,40,44] may be harnessed to process information.[31–35] Local nanomagnet switching has been achieved through diffraction-limited heat-assisted reversal, relying on global fields in conjunction with laser illumination[2,45] and by cumbersome field-assisted[46] and field-free scanning-probe[41,47,48] techniques. In the latter, the magnetic field from a magnetic tip breaks the nanomagnet symmetry, causing transient domain wall formation and asymmetric propagation, leading to switching.[48] Realizing rapid low-power single-element magnetic switching is pivotal for the development of functional nanomagnetic computation and storage devices.

Here, we demonstrate deterministic AOMS in both isolated nanomagnets and dense square artificial spin ice (ASI)[36,49,50] arrays using simple NiFe alloys and nanofocused low-power (approximately 2.74 mW), linearly polarized continuous-wave (CW) lasers with no external magnetic fields applied. Under certain conditions, the optical excitation leads to an asymmetric absorption across the nanomagnet, breaking the system symmetry and providing a driving force for switching. Despite the long exposure times (measured in milliseconds) a single, deterministic toggle switch, or magnetic inversion, occurs. This switching is distinct from helicity-dependent switching, which is magnetic field-like and writes a specific magnetization

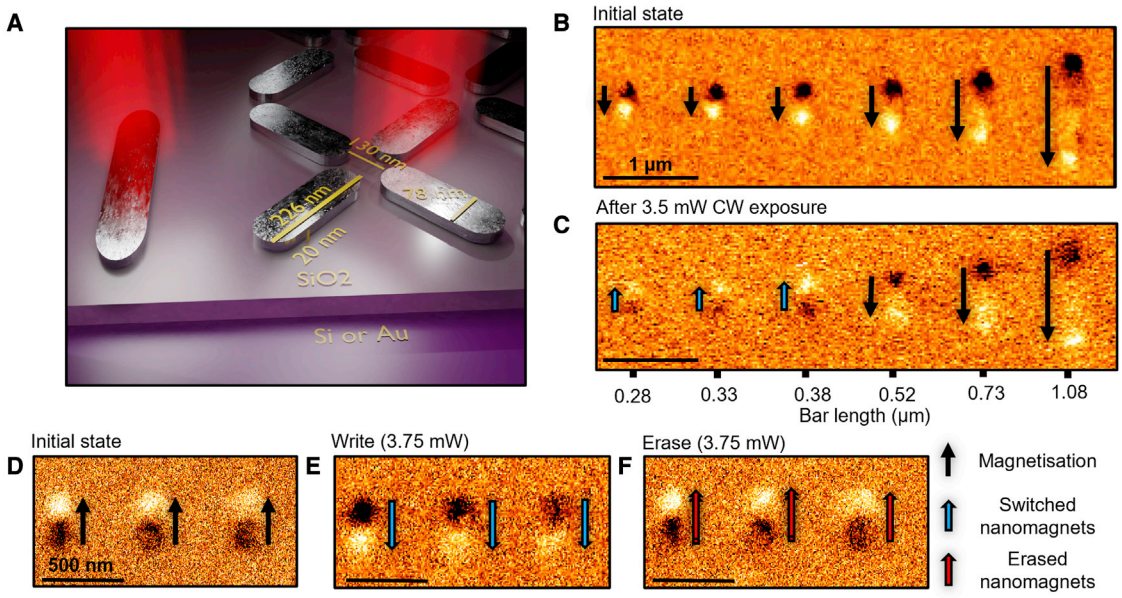


**Figure 1. Switching isolated nanomagnets**

(A) Schematic of linearly polarized CW laser exposure of isolated nanomagnets (left) and densely packed Py (NiFe) nanomagnets in a square ASI (right) patterned on Si or Au substrates with a $SiO_2$ coating. MFM images of isolated nanomagnets patterned on an Au (250 nm)/$SiO_2$ (290 nm) substrate (B) in the saturated state and (C) after linearly polarized CW laser exposure at 3.5 mW power. Scale bars in B and C are equal to 1 μm. Bars with length ($L$) ≤ 380 nm switch. MFM images of (D) three nanomagnets with $L$ = 280 nm in an initial saturated state.

(E) Subsequent switching after linearly polarized CW exposure with 3.75 mW.

(F) Switching after a second 3.75 mW exposure demonstrating the ability to rewrite/erase previously written states. In each case laser polarization is parallel to the long axis of nanomagnets and the laser scans perpendicular to the bar long axis. Scale bars in D–F are equal to 500 nm.

direction, implying that our observed switching is a result of transient dynamics as the system approaches thermodynamic equilibrium. Tuning the geometry and dimensions of magnetic/di-electric samples can produce significant enhancements of a number of magneto-optical effects, such as enhanced Kerr rotation.[51,52] Additionally, coupling magnetic systems with optical structures can lead to enhanced light absorption.[53,54] The substrates (here $Si/SiO_2$ or $Au/SiO_2$) on which the nanomagnets are situated have an anti-reflection function, which enhances optical absorption within the nanomagnets up to 65% of the total incident light across a broad frequency range. Sub-diffraction writing and erasing of information is achieved in single nanomagnets. All square-ASI vertex configurations are deterministically written, from low-energy ground states to high-energy monopole-like states, irrespective of their dipolar energies, ruling out thermal relaxation. Switching is not observed in Co or Ni nanostructures, suggesting that multi-species interactions play a role in the reversal mechanism. Our results open up intriguing questions into the manipulation of nanostructured ferromagnets with linearly polarized light and usher in a new paradigm of low-power magnetization control with vast implications across data storage, computation, and magnonics.

## RESULTS AND DISCUSSION

### Deterministic reversal of isolated nanomagnets

Figure 1A shows a schematic of nanomagnets exposed with a focused linearly polarized CW laser. We first consider reversing isolated $Ni_{81}Fe_{19}$ (permalloy [Py]) nanomagnets separated by 1 μm, such that dipolar interactions are negligible. The nanomagnets are patterned on top of an Au (250 nm)/$SiO_2$ (290 nm) substrate that displays enhanced optical absorption (see Supplementary note 1 and

Figures S1 and S2). Figure 1B shows a before magnetic force microscopy (MFM) image of field-saturated nanomagnets with lengths $L$ = 0.28–1.08 μm. Each bar exhibits a positive (light) and negative (dark) magnetic charge, indicating magnetization direction, shown by adjacent arrows. Figure 1C shows the same bars after exposure to a λ = 633 nm linearly polarized (parallel to nanomagnet long axis) CW laser with 580 nm diameter spot and 3.5 mW power, swept across the nanomagnets perpendicular to their long axis. Magnetic switching is observed in the three leftmost bars (L ≤ 0.28–0.38 μm), indicated by light-blue arrows. Figures 1D–1F demonstrate write/erase functionality in three L = 0.28 μm bars. Bars are initially globally saturated (Figure 1D), then exposed to a λ = 633 nm, 3.75 mW power linearly polarized CW laser such that all bars switch (write) (Figure 1E). All bars then switch back following a second exposure (erase) (Figure 1F). The observation of toggle-switching functionality implies that the underlying mechanism is not magnetic field-like, because repeating the same write operation inverts the magnetization each time. Note that powers stated are measured before focusing and 90% or less of the power reaches the sample (see Methods for details).

### Deterministic reversal in ASI networks

We now further explore the exposure of strongly interacting, sub-diffraction limited nanomagnets arranged in a dense square ASI, patterned on a $Si/SiO_2$ (300 nm) substrate. This substrate was selected to demonstrate the efficacy of the switching technique on commercially available, sub-optimal substrates (no additional absorption-enhancing Au layer) (Supplementary note 1 and Figures S1 and S2). Strong interactions between neighboring nanomagnets lead to four vertex types with differing energies[49] (Figure 2A), providing a challenging proving ground for local magnetic control as strong dipolar interactions will oppose writing of high-energy states. Figure 2A shows all possible vertex configurations in square ASI in order of increasing energy, labeled types 1–4 (vertex energies detailed in Supplementary note 4 and Figure S6). Figure 2B shows an scanning electron microscopy image of the ASI array. Nanomagnet dimensions are $L$ = 226 nm, $W$ = 78 nm, and $P$ = 356 nm (further scanning electron microscopy images are provided in Supplementary note 2 and Figure S3).

First, we consider exposing ASI to discrete spot illuminations of a λ = 633 nm, 5 mW CW laser for approximately 0.25 s. The laser position is static throughout illumination. Laser focal spot size is 580 nm. Before exposure, the ASI is initialized via global-field saturation ($-x$, $+y$) to define an array of type 2 vertices (Figure 2C). Figure 2D shows the array microstate after grid-like spot exposures with a variety of laser polarizations. Here, points on a grid with a separation of 2 μm are illuminated for approximately 0.25 s. Laser polarization governs the resultant written vertex state, with color-coded regions of Figure 2D shown zoomed in in Figures 2E–2L. Higher powers and longer illuminations lead to sample damage (not shown). The zoomed regions show successful writing of ASI vertex types 1 (Figures 2I and 2J), 3 (Figures 2E and 2F), and 4 (Figures 2K and 2L) (Figures 2G and 2H are from a different region of the array). Note that the MFM images are supplemented with magnetic charge schematics and the corresponding laser polarizations required to prepare each state, indicated above each MFM image. When illuminating the array at a single spot (Figures 2E–2H), a single nanomagnet with the long axis parallel to the laser polarization switches. This selectivity arises from the polarization-dependent absorption (see Supplementary note 1 and Figure S1). This forms a high-energy state, comprising a pair of type 3 vertices. Two subsequent $\hat{x}$ then $\hat{y}$-polarized exposures results in two nanomagnets switching (one from each $x$, $y$ subset). Here, both low-energy type 1 (Figures 2I, 2J) and high-energy type 4 (Figures 2K, 2L) vertices may be written. The position of the incident laser with respect to the surrounding

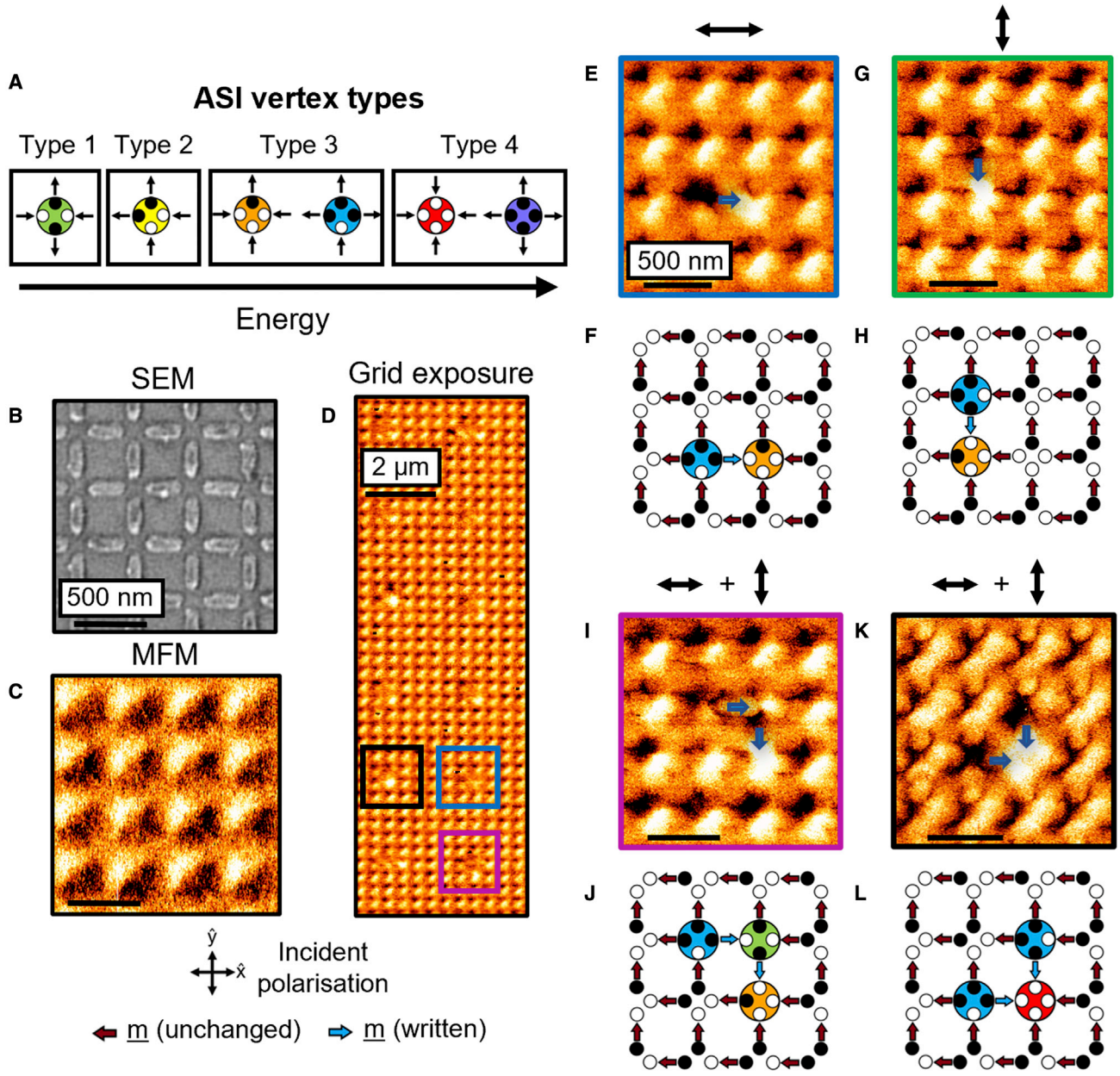


**Figure 2. Single nanomagnet switching in a dense array**

(A) Vertex types in square ASI.

(B) Scanning electron microscopy (SEM) image of a square ASI array.

(C) MFM images of an equivalent array after global-field initialization along $-x,+y$. Scale bars in B and C are equal to 500 nm.

(D) MFM image showing a grid of reversals after $\lambda = 663$ nm laser exposure with a 580-nm focal spot at 5 mW for approximately 0.25 s. (E–L) Scale bar is equal to 2 μm. Zoomed-in MFM images and schematics of color-coded regions of (D) showing nanomagnet reversal after laser exposure with (E, F) $\hat{x}$ polarization, (G, H) $\hat{y}$ polarization, I–L) $\hat{x}$ then $\hat{y}$ polarization. (G) Comes from a different region of the array. The single polarization exposure in (E–H) result in a pair of type 3 vertices. When exposing both polarizations, both (I, J) type 1 (GS) and (K, L) high-energy T4 (MP) vertices can be prepared depending on which nanomagnets are exposed. (E–L) Scale bar, 500 nm. Only written vertices are colored. Scale bars in (E–L) are equal to 500 nm.

microstate determines whether a type 1 or type 4 is written. The ability to write type 4 vertices strongly suggests that switching occurs in a deterministic manner, rather than via nanomagnet thermalization and relaxation, which would strongly favor the system's ground state and that dipolar interaction does not affect switching.

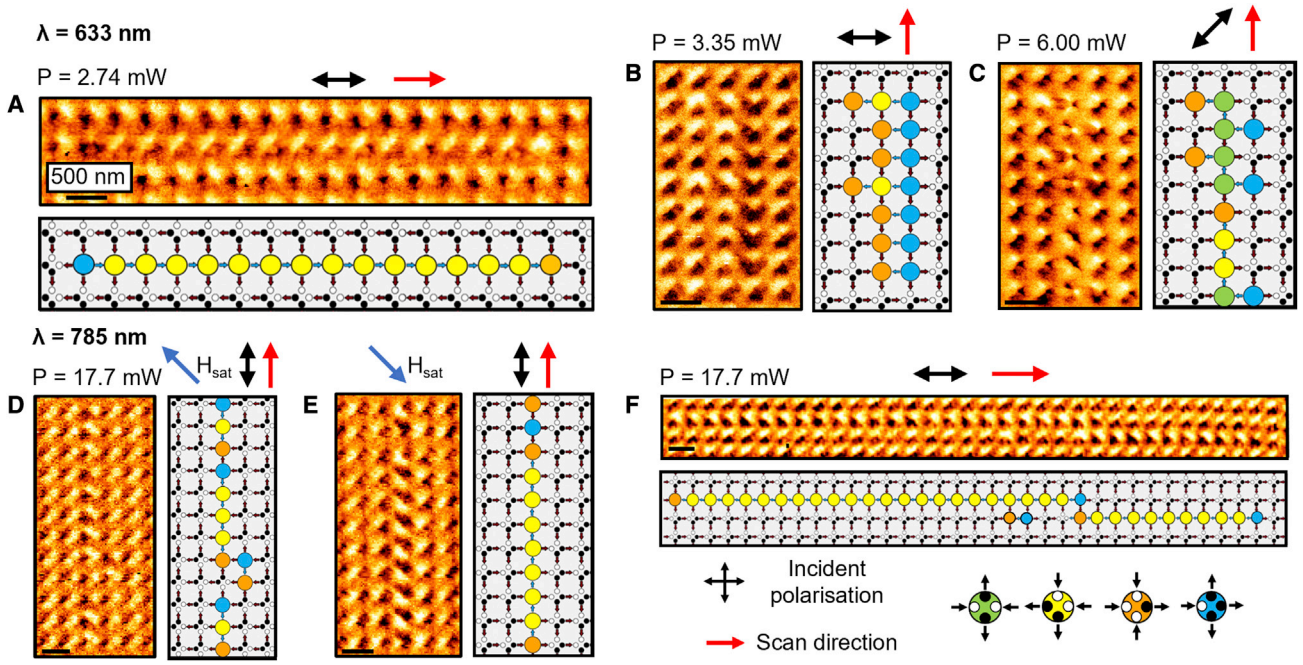


**Figure 3. Multiple island switching in dense arrays**

(A–C) MFM images of switching chains after exposure to λ = 633 nm scanning laser with (A) polarization ‖ scan direction writing a chain of type 2 vertices (B) polarization ⊥ scan direction writing a chain of type 3 vertices and (C) polarization at 45° to the scan direction where both subsets of bars are exposed to the same incident power and both subsets are written.

(D and E) MFM images and schematics of switching via λ = 785 nm after saturating the array in opposite directions. Type 2 chains are written in both cases, ruling out the effect of stray field, which would assist switching in one case and oppose switching in the other.

(F) MFM images and schematics after exposure to a λ = 785 nm laser with polarization ‖ scan direction. Similar writing characteristics to the shorter wavelength but at approximately a six times power increase because of the lower absorption at this wavelength. Scale bars are equal to 500 nm.

This Gaussian distribution of power across the beam gives an FWHM of approximately 340 nm. Combining this with selectivity enabled by the polarization-dependent absorption predominantly results in a single nanomagnet switching during each exposure. We observe an approximately 20% chance of switching two nanomagnets with the same polarization, which may be decreased by using larger nanomagnets or a smaller design wavelength. The observed writing of low and high-energy states with single-nanomagnet precision shows a deterministic reversal mechanism and illustrates the applicability of this method to next-generation storage and memcomputing.

We now explore switching when scanning the laser spot across the array. Here, the beam traverses the entire 30 μm array at 20 μm/s once, exposing each nanomagnet for approximately 18 ms. The relative angle between the polarization and the scan direction is either 0°, 45°, or 90°. Figure 3 shows MFM images and corresponding magnetization schematics of line-scanned writing exposures at laser wavelengths of 633 nm (Figures 3A–3C) and 785 nm (Figures 3D–3F). At a 633 nm wavelength, switching occurs at laser powers as low as 2.74 mW, whereas 785 nm wavelength switching has an optimum power of 17.7 mW; this is due to the wavelength-dependent absorption of the nanomagnetic array (Supplementary note 1 and Figure S1) and is higher than expected because of the wavelength-dependent optical losses in the experimental setup (see Methods). For ASI fabricated on Au/$SiO_2$ substrates with higher total absorption, we observe switching across a wider range of nanomagnet dimensions ($\lesssim$1 μm bar length) at similar laser powers (Supplementary note 5 and Figure S7).

Parallel polarization and line-scan direction (Figures 3A, 3D–3F) gives rise to long chains of switches where adjacent nanomagnet reversals share a common vertex. Lines written in this configuration comprise a chain of type 2 vertices (yellow circles) with a single type 3 vertex at either end (blue and orange circles). Other than creating the type 3 vertex pair, system energy is not increased as the written type 2 vertices are equal in energy to the initial saturated type 2 background state. Furthermore, the orientation between the scan direction and the nanomagnet means that one end of the bar is always exposed first, maximizing the asymmetry in the absorption. Within one scan, up to 22 consecutive island reversals are observed in this configuration. Perpendicular polarization and scan direction (Figure 3B) results in a type 3 vertex pair at every point on the line scan (as observed in the static exposures Figures 2D–2H), continually increasing system energy. In one laser scan, up to seven consecutive island reversals are observed in this configuration, demonstrating strong reversal control over highly energetically unfavorable states. If the laser polarization is oriented 45 ° to the scan direction (Figure 3C), both $x, y$ subsets receive equal power and both can switch, resulting in a chain of type 1 vertices (green circles). Here, approximately 2× power is required, as expected.

No magnetic fields are applied during writing and Hall probe measurements reveal stray fields below 1 Oe at the sample. Figures 3D, 3E show MFM images and vertex-type schematics after saturating the same array in opposite initial directions and exposing to a scanning beam ($\lambda$ = 785 nm) with polarization parallel to the scan direction. Any unintended stray field in the experimental setup that assists reversal in one direction will oppose reversal in the other. Crucially, switching is observed in both cases, ruling out the role of external fields in switching.

Our results demonstrate deterministic and rewriteable AOMS in isolated and densely packed nanomagnets. Our methodology requires no external field and operates using simple CW lasers operating at low-power (2.74–6 mW) and low power densities (1.04–2.27 MW/cm$^2$ for a 580 nm spot). The switching is consistent across multiple samples and is, therefore, robust against fabrication imperfections. The absorption profiles allow for attractive optical read/write functionality whereby writing is performed at a wavelength near the peak absorption and reading, via magneto-optical Kerr effect microscopy, is performed with a second laser at a wavelength far from the absorption peak. We do not observe any significant sample degradation at optimum powers. In general, we observe a range of responses depending on laser power. At low powers ($<P_1$), no switching and no degradation is observed. At intermediate powers ($P_1$–$P_2$), we observe switching with no degradation (e.g., Figures 2 and 3). At higher powers we observe switching accompanied by damage ($P_2$–$P_3$) and at very high powers we observe significant degradation ($>P_3$). Sample degradation occurs because of oxidation and diffusion effects from heating. The exact values of $P_1$, $P_2$, and $P_3$ depend on the sample and the geometry of the nanomagnets.

### Reversal mechanism

The all-optical switching mechanism requires strong polarization-dependent absorption of light in the nanomagnets, as well as the existence of an asymmetry to provide a driving force for reversal. The size and shape of the nanomagnets thus have dual roles, controlling both magnetic behavior and the polarization-dependent optical absorption. Absorption is strongest when polarized along the nanomagnet long axis, giving selectivity of different bar subsets as observed in Figures 2 and 3. There are three light absorption mechanisms: the plasmonic antenna resonance, a plasmonic grating effect due to the in-plane nanoarray periodicity, and the interference effect of reflection from the substrate-silica interface. We find

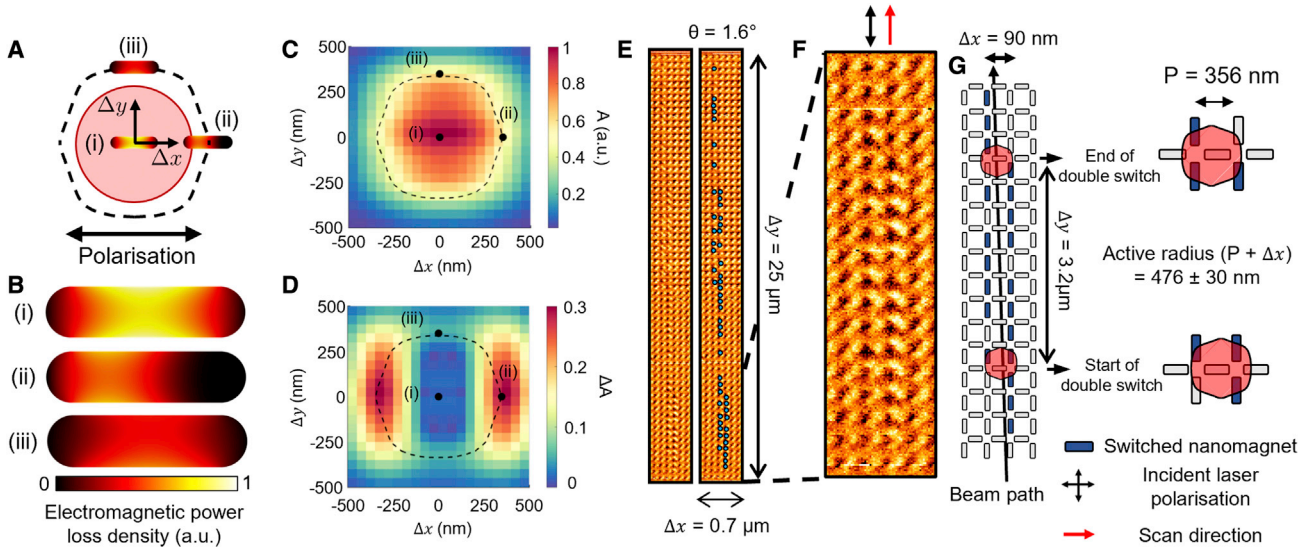


**Figure 4. Enhanced asymmetric absorption**

(A) Simulation schematic whereby a nanomagnet is shifted relative to a central Gaussian beam with a diameter of 580 nm.

(B) Absorption profiles of the three positions marked in (A). Asymmetric absorption profiles are observed when the beam is off center.

(C) Simulated normalized absorption and (D) asymmetry factor $\Delta A(\Delta x, \Delta y)$ for varying shifts, $\Delta x$ and $\Delta y$. The dashed shape indicates 50% total absorption. Nanomagnet dimensions of $L$ = 226 nm, $W$ = 78 nm, and $t$ = 20 nm are used.

(E) MFM images (raw and annotated) of a chain of reversals when scanning in $y$ with an offset of 1.6°. Blue dots correspond to reversed nanomagnets. Two regions of single and double line switches are observed.

(F) Zoomed in MFM image and (G) schematic of region with two columns of switching. At a 1.6° angle, the two regions of double switching lasts for 3.2 and 5.2 μm in the $y$ direction during which the beam moves 90 and 140 nm in x. This gives an active region of 476 ± 30 nm within which nanomagnets can switch.

the latter mechanism dominates (see Supplementary note 3 and Figures S4 and S5). This is to our advantage; this mechanism allows design freedom over the nanomagnet dimensions and array geometry, as well as greater tolerance to nanofabrication imperfections. Our choice of substrate significantly enhances the total absorption in the nanomagnet up to 16.25 times compared with conventional Si substrates (see Supplementary note 1 and Figures S1 and S2).

A key role is played by the location of the laser spot relative to each nanomagnet. We have computed the absorption, $A(\Delta x, \Delta y)$, of light in the Py layer of a nanomagnet in a Gaussian beam, where $\Delta x$ and $\Delta y$ are displacements relative to a fixed beam, as shown in Figure 4A. The Gaussian beam has a waist diameter of 580 nm at the sample, which matches experimental conditions. We also compute the absorption in four quadrants of the nanomagnet, to evaluate the degree of absorption asymmetry $\Delta A(\Delta x, \Delta y)$ (see Methods). Figure 4B shows the absorption profiles for three nanomagnet positions. For the central nanomagnet position (i), the absorption is localized in the center of the nanomagnet. As the nanomagnet is shifted (ii, iii), the absorption profile becomes asymmetric, providing a driving force for magnetic reversal (the implications of this asymmetry are discussed later). Figures 4C and 4D show the simulated absorption and absorption asymmetry factor, both normalized to the peak absorption, $A(0, 0)$. Asymmetric absorption is a strong effect, with more than 50% of peak absorption occurring at peak asymmetry. This implies that one side of the nanomagnet absorbs approximately four times more than the other side. The asymmetric absorption grows for larger displacements, but with diminishing total absorption. Thus, the effect of asymmetry is strongest within the illustrated dotted line boundaries of Figures 4C and 4D, where the absorption is

more than 50% of the peak value. The shape of the absorption profile (dotted line) is a convolution between the circular beam and bar-shaped nanomagnet. When the polarization is aligned perpendicular to the bar long axis, the same asymmetry profile is observed, but with a decrease in total absorption (Supplementary note 6 and Figure S8).

When applied to ASI arrays, nanomagnet switching is affected by polarization and scan direction. Figure 4E shows an MFM image, raw (left) and annotated to highlight reversal (right), after scanning a laser along an ASI array. Here the polarization is aligned in $\hat{y}$. The beam traverses 0.7 μm and 25 μm in $x$ and $y$, respectively, with an angular offset of 1.6°. Two regions of double column switching are observed with lengths of 3.2 μm and 5.2 μm in $y$. Figure 4 shows (F) an enlarged MFM image and (G) the schematic of a region where two columns of switches occur (switched nanomagnets are shaded blue). From the angular offset, we deduce that the beam traverses 90 nm and 140 nm in $x$, respectively, during these regions. From this we can approximate the diameter $D$ of the active region of the beam using $D = \Delta x + P$ where $P$ is the period of the ASI array. This gives an active region of $D = 476 \pm 30$ nm, slightly smaller than the simulated region of 50% absorption in Figure 4C. As such, when scanning parallel to the polarization and bar long-axis, a single line of nanomagnets can be switched as $D < 2P$, meaning that only one column of bars is illuminated. This is consistently observed throughout Figure 3. However, when the scan direction is perpendicular to the polarization, multiple columns of nanomagnets are seen to switch approximately 20% of the time, as shown in Figure 3B. We attribute this to the structure of the asymmetric absorption profile in Figure 4D. While the two regions of asymmetry move one after the other for scan direction and polarization aligned, they move side by side for the perpendicular case. This results in a higher switching yield when scanning parallel to the polarization, as observed in Figures 3A and 3B. The broader reach of the asymmetry in the latter case is consistent with the observation of multiple switched lines. Further evidence of the key role played by the asymmetry is found in the switching fidelity when scanning parallel to the polarization. In this configuration, one end of the nanomagnet is preferentially excited, maximizing asymmetry. We consistently observe greater writing fidelity in this mode of operation. As such, there is strong evidence that the asymmetric absorption provides the driving force for reversal. A result of the asymmetric absorption is the presence of a temperature gradient across the length of the nanomagnet, during the initial stages of excitation, which can facilitate the flow of magnons, spin currents,[55] and domain walls.[56]

The existence of asymmetry in the writing process alone is not sufficient to explain the cause of reversal. There must be an additional microscopic mechanism that is capable of deterministically inverting the magnetization during each illumination. Here, we begin with a process of deduction. The deterministic switching into any allowed magnetic state with the same sample mounting as illustrated in Figures 3D, 3E excludes field-driven heat-assisted switching (as in Pancaldi et al.[2]) from unintentional stray fields in our system. Our deterministic findings are also not consistent with stochastic thermal switching effects from heating nanomagnets beyond the Curie temperature $T_c$ or superparamagnetic limit. The written high-energy, low-entropy monopole defect states are never favored by thermalisation.[48] The observed switching fidelity in Figure 3F of 22 consecutive switches has a corresponding thermalization probability of $0.5^{22} = 2.3 \times 10 - 7$. We anticipate that the low-power illumination would not heat the lattice temperature above 380 $K^2$. Magnetometry measurements of a 2 × 2 mm ASI array with equivalent dimensions reveals only an approximate 10% decrease in the magnetization is observed between 120 and

380 K, implying that we are not heating close to $T_c$ for these nanomagnet samples (Supplementary note 7 and Figure S9).

We observe a single, deterministic reversal for each exposure as opposed to multiple switches across approximately millisecond timescales. The inverse Faraday effect and dichroism effects are ruled out, both because of the linearly polarized exposure and the deterministic inversion functionality we observe. Helicity-dependent effects have a magnetic field-like symmetry breaking and so write a specific magnetization direction, with no effect if the magnetization is already in that direction, unlike our observed toggling. As such, it is likely that the microscopic process involves transient dynamics during the initial stages of excitation when the temperature gradient arising from asymmetric absorption is maximum, that is, as the system is approaching thermodynamic equilibrium. It is plausible that, during the initial exposure, the electron and spin temperatures at the ends of the nanomagnets increase rapidly, as observed in a number of AOMS studies,[13] leading to rapid demagnetization. Magnetization reversal may then proceed via transient spin currents, magnon generation and propagation, or domain wall propagation along the absorption-induced temperature gradient. Another possibility is spin redistribution through dynamic changes in the spin bands. There has been recent theoretical and experimental evidence of optically induced spin transfer (OISTR) in ferromagnetic alloys[57–59] whereby incoming photons may excite electrons between spin minority bands of a heterogeneous material provided that the band structure satisfies necessary requirements. Specifically, there should be an available transition between two spin minority bands at the incident photon energy and no available transitions in the spin majority bands. These studies do not observe switching, yet single-pulse HIS is observed in Co/Pt multilayers,[26] which possess the necessary band structure.[60] The phenomenon is general to all multi-component magnetic media[59] and therefore strong in $Ni_{50}Fe_{50}$,[57] more so than $Ni_{81}Fe_{19}$, but not present in Co or Ni.

To test our working hypothesis that the observed AOMS is driven by a plasmonically enhanced OISTR mechanism, we fabricated a set of $Ni_{50}Fe_{50}$ (20 nm thickness), Co (8 nm thickness), and Ni (20 nm thickness) nanomagnetic arrays patterned on a $Au/SiO_2$ substrate (Supplementary note 8 and Figure S10), with the prediction that switching fidelity/power threshold would be as good or better in $Ni_{50}Fe_{50}$ and significantly worse in pure Co and Ni. A lower Co thickness is used to give a roughly equivalent bar magnetization. Both predictions were confirmed in the subsequent experiments. For $Ni_{50}Fe_{50}$, isolated nanomagnet switches were observed at 3 mW (approximately a 14% decrease in power) across a broader range of nanomagnet dimensions compared to $Ni_{81}Fe_{19}$. Conversely, no switches were observed in Co nanostructures up to incident powers of 30 mW and Ni nanostructures up to 8 mW, consistent with the OISTR process. Both Co and Ni nanostructures become damaged at approximately 7 mW, meaning that the necessary power to observe switching has been trialed. Previous OISTR studies focus on ultrafast spin dynamics, and the effects over longer timescales remain unknown. The use of CW exposure, as opposed to ultrafast, suggests that OISTR may both stronger and persist for longer than previously expected, highlighting the need for dedicated studies at longer timescales. Although OISTR alone cannot cause switching, the rapid redistribution of spins during the initial transient stages of excitation may be sufficient to nucleate a reversal.

In summary, we have demonstrated selective and deterministic AOMS of individual and densely packed ferromagnetic nanostructures using a linearly polarized, low-power CW laser. We achieve sub-diffraction limit, single nanomagnet

switching of diverse ASI microstates including thermally unfavorable high-energy configurations. Our observation of toggle switching, or deterministic inversion, strongly implies a symmetry-breaking driving force, but is not consistent with a magnetic field-like force. The optical excitation and absorption within the nanomagnet are strongly asymmetric, yielding a transient temperature gradient and other transient dynamics. This raises fascinating questions about the microscopic reversal mechanism and many avenues for future work. Our results demonstrate high-power ultrafast excitation is not a prerequisite to AOMS, and highlight the need for magneto-optic studies across longer time frames. The materials employed are cheap and earth abundant, and we expect switching functionality to be retained across a broad range of substrate and ferromagnetic materials making the technique saleable and highly compatible with existing technologies. The low-power consumption and cheap cost of the non-specialized CW laser have profound implications across a host of device technologies including data storage, magnonics, and non-conventional computing functionalities, particularly neuromorphic and memcomputing hardware.

## EXPERIMENTAL PROCEDURES

### Resource availability

#### *Lead contact*

Further information and requests for resources should be directed to and will be fulfilled by the lead contact, Kilian D. Stenning (k.stenning18@imperial.ac.uk).

#### *Materials availability*

The materials used during this study are available from the lead author upon reasonable request.

#### *Data and code availability*

The data and code used/analyzed during this study are available from the lead author upon reasonable request.

### Simulation details

The numerical simulations of asymmetric absorption were carried out using the finite element method technique (COMSOL Multiphysics). To simulate a Gaussian beam with the diffraction limited spot size, the paraxial Gaussian beam formula was applied along the negative *z*-direction in our simulation. The incidence is polarized in the *x*-direction with its focus point at the structure-substrate interface. In this simulation, a single nanomagnet with dimensions of $L$ = 226 nm, $W$ = 78 nm, and $t$ = 20 nm are used. We also include a 20 nm $Al_2O_3$ capping on either side of the Py layer to match experimental conditions. The nanomagnet is positioned on the top of a $Si/SiO_2$ (300 nm) substrate with its long axis along the *x*-direction. In all directions, perfectly matched layer boundary conditions were applied to absorb incident light with minimal reflections. To simulate the normalized absorption and the asymmetric absorption, the nanomagnet is separated into left-upper, left-bottom, right-upper, and right-bottom parts, and the absorption of the Py layer in these four parts of the nanomagnet corresponding with different displacements, namely, $A_{l,u}(\Delta x,\Delta y)$, $A_{l,b}(\Delta x,\Delta y)$, $A_{r,u}(\Delta x,\Delta y)$, and $A_{r,b}(\Delta x,\Delta y)$, is calculated. The absorption of the left and right half sides of the nanomagnet were calculated using $A_l(\Delta x,\Delta y) = A_{l,u}(\Delta x,\Delta y) + A_{l,b}(\Delta x,\Delta y)$ and $A_r(\Delta x,\Delta y) = A_{r,u}(\Delta x,\Delta y) + A_{r,b}(\Delta x,\Delta y)$. The absorption of the upper and bottom half sides of the nanomagnet were calculated using $A_u(\Delta x,\Delta y) = A_{l,u}(\Delta x,\Delta y) + A_{r,u}(\Delta x,\Delta y)$ and $A_b(\Delta x,\Delta y) = A_{l,b}(\Delta x,\Delta y) + A_{r,b}(\Delta x,\Delta y)$. The asymmetry was then calculated as $\Delta A(\Delta x,\Delta y) = \sqrt{(A_l(\Delta x,\Delta y) - A_r(\Delta x,\Delta y))^2 + (A_u(\Delta x,\Delta y) - A_b(\Delta x,\Delta y))^2}$. The incident wavelength

is 633 nm. The refractive indexes of the $Al_2O_3$, Py, $SiO_2$, Si are set 1.7662, 2.3813–3.9415i, and 1.4570, 3.8813–0.0189i, respectively.

### Sample fabrication

Samples were fabricated via electron beam lithography with liftoff on a Raith eLine system with a bilayer 495K/950K PMMA resist. Si substrates with a 300 nm $SiO_2$ layer were purchased commercially. The Au substrates were deposited on an $Si/SiO_2$ substrate with the following thicknesses (nm): Cr(2)/Au(250)/Cr(2)/$SiO_2$ (290). Cr is used to aid Au adhesion. $Al_2O_3$, $Ni_{81}Fe_{19}$, $Ni_{50}Fe_{50}$, and Co were thermally evaporated at a base pressure of $2\times10^{-6}$ mbar. For samples fabricated on $Si/SiO_2$, a 15-nm $Al_2O_3$ layer is deposited on either side of the nanomagnet to protect against oxidation. For samples fabricated on $Au/SiO_2$ substrates, a 4 nm $Al_2O_3$ coating on the top layer is used to protect oxidation. The presence and thickness of $Al_2O_3$ does not significantly affect light absorption.

### MFM

Magnetic force micrographs were produced on a Dimension 3100 using commercially available low-moment and normal-moment MFM tips.

### Illumination experiments

Laser illumination by continuous wave lasers with different wavelengths (633 nm and 785 nm) were focused to a diffraction limited spot on the sample through a confocal Raman microscope (alpha300 RSA+, WITec). The light was linearly polarized and focused by a 100 × (NA = 0.9) (Zeiss) microscope objective. The focal spot was scanned to illuminate the locations of interest. To achieve the fastest line scanning speed, the instrument was simply scanned between two pre-defined points. For slower scans, 50 points were defined along each scan line and the detector integration time was used to control the dwell time. It should be noted that the integration time is usually used to control spectra collection, but here this parameter controls the illumination time. The power of the beam was measured by a power meter (PM100D) (Thorlabs) attached to the objective turret and all powers stated are measured before focusing. The power transmitted through the objective is 90% or less, and may be lower because of optical losses in the set up. Measurements suggest that approximately 65% and approximately 45% of the power may be reaching the sample at wavelengths of 633 nm and 785 nm, respectively.

## SUPPLEMENTAL INFORMATION

Supplemental information can be found online at https://doi.org/10.1016/j.xcrp.2023.101291.

## ACKNOWLEDGMENTS

This work was supported by the Leverhulme Trust (RPG-2017-257) to W.R.B. and the Engineering and Physical Sciences Research Council (Grant No. EP/W524335/1) to K.D.S. J.C.G. was supported by the Royal Academy of Engineering under the Research Fellowship program. A.V. was supported by the EPSRC Center for Doctoral Training in Advanced Characterisation of Materials (Grant No. EP/L015277/1). X.X. was supported by the EPSRC (Engineering and Physical Sciences Research Council) (Grant No. EP/M013812/1). The authors thank Lesley F. Cohen of Imperial College London, Naëmi Leo of Universidad de Zaragoza, and Tom Hayward of The University of Sheffield for enlightening discussion and comments, and David Mack for excellent laboratory management.

## AUTHOR CONTRIBUTIONS

K.D.S., X.X., J.C.G., R.O., and W.R.B. conceived the work. K.D.S. drafted the manuscript other than the description of the absorption, with contributions from all authors in editing and revision stages. X.X. and R.O. drafted the description of the absorption section. K.D.S., J.C.G., A.V., O.K., and H.H. fabricated the ASI. X.X. and H.H. performed the laser illumination protocols. K.D.S., H.H., A.V., and J.C.G. performed MFM measurements. X.X. performed FTIR measurements, simulations, and absorption calculations. K.D.S., A.V., and J.C.G. performed magnetometry measurements. K.D.S. performed simulations of vertex energies. K.D.S. created CGI images.

## DECLARATION OF INTERESTS

Authors patent applicant. Inventors (in no specific order): K.D.S., X.X., J.C.G., H.H.H., R.F.O., W.R.B. Application number: 2117279.6. Application filed. Patent covers the all-optical magnetic switching technique.

Received: August 15, 2022
Revised: December 21, 2022
Accepted: January 25, 2023
Published: February 15, 2023

## REFERENCES

1. Kovalenko, V.F., and Nagaev, É.L. (1986). Photoinduced magnetism. Sov. Phys. Usp. *29*, 297–321.

2. Pancaldi, M., Leo, N., and Vavassori, P. (2019). Selective and fast plasmon-assisted photo-heating of nanomagnets. Nanoscale *11*, 7656–7666.

3. Kryder, M.H., Gage, E.C., McDaniel, T.W., Challener, W.A., Rottmayer, R.E., Ju, G., Hsia, Y.-T., and Erden, M.F. (2008). Heat assisted magnetic recording. Proc. IEEE *96*, 1810–1835.

4. Stanciu, C.D., Hansteen, F., Kimel, A.V., Kirilyuk, A., Tsukamoto, A., Itoh, A., and Rasing, T. (2007). All-optical magnetic recording with circularly polarized light. Phys. Rev. Lett. *99*, 047601.

5. Kirilyuk, A., Kimel, A.V., and Rasing, T. (2010). Ultrafast optical manipulation of magnetic order. Rev. Mod. Phys. *82*, 2731–2784.

6. Kimel, A.V., and Li, M. (2019). Writing magnetic memory with ultrashort light pulses. Nat. Rev. Mater. *4*, 189–200.

7. Maccaferri, N., Zubritskaya, I., Razdolski, I., Chioar, I.-A., Belotelov, V., Kapaklis, V., Oppeneer, P.M., and Dmitriev, A. (2020). Nanoscale magnetophotonics. J. Appl. Phys. *127*, 080903.

8. El Hadri, M.S., Pirro, P., Lambert, C.-H., Petit-Watelot, S., Quessab, Y., Hehn, M., Montaigne, F., Malinowski, G., and Mangin, S. (2016). Two types of all-optical magnetization switching mechanisms using femtosecond laser pulses. Phys. Rev. B *94*, 064412.

9. Medapalli, R., Afanasiev, D., Kim, D.K., Quessab, Y., Manna, S., Montoya, S.A., Kirilyuk, A., Rasing, T., Kimel, A.V., and Fullerton, E.E. (2017). Multiscale dynamics of helicity-dependent all-optical magnetization reversal in ferromagnetic co/pt multilayers. Phys. Rev. B *96*, 224421.

10. Ellis, M.O.A., Fullerton, E.E., and Chantrell, R.W. (2016). All-optical switching in granular ferromagnets caused by magnetic circular dichroism. Sci. Rep. *6*, 30522.

11. Lambert, C.-H., Mangin, S., Varaprasad, B.S.D.C.S., Takahashi, Y.K., Hehn, M., Cinchetti, M., Malinowski, G., Hono, K., Fainman, Y., Aeschlimann, M., and Fullerton, E.E. (2014). All-optical control of ferromagnetic thin films and nanostructures. Science *345*, 1337–1340.

12. Kichin, G., Hehn, M., Gorchon, J., Malinowski, G., Hohlfeld, J., and Mangin, S. (2019). From multiple-to single-pulse all-optical helicity-dependent switching in ferromagnetic co/pt multilayers. Phys. Rev. Appl. *12*, 024019.

13. Ostler, T., Barker, J., Evans, R., Chantrell, R., Atxitia, U., Chubykalo-Fesenko, O., El Moussaoui, S., Le Guyader, L., Mengotti, E., Heyderman, L., et al. (2012). Ultrafast heating as a sufficient stimulus for magnetization reversal in a ferrimagnet. Nat. Commun. *3*, 666.

14. Stanciu, C.D., Tsukamoto, A., Kimel, A.V., Hansteen, F., Kirilyuk, A., Itoh, A., and Rasing, T. (2007). Subpicosecond magnetization reversal across ferrimagnetic compensation points. Phys. Rev. Lett. *99*, 217204.

15. Radu, I., Vahaplar, K., Stamm, C., Kachel, T., Pontius, N., Dürr, H.A., Ostler, T.A., Barker, J., Evans, R.F.L., Chantrell, R.W., et al. (2011). Transient ferromagnetic-like state mediating ultrafast reversal of antiferromagnetically coupled spins. Nature *472*, 205–208.

16. El Hadri, M.S., Hehn, M., Malinowski, G., and Mangin, S. (2017). Materials and devices for all-optical helicity-dependent switching. J. Phys. D Appl. Phys. *50*, 133002.

17. Le Guyader, L., El Moussaoui, S., Buzzi, M., Chopdekar, R.V., Heyderman, L.J., Tsukamoto, A., Itoh, A., Kirilyuk, A., Rasing, T., Kimel, A.V., and Nolting, F. (2012). Demonstration of laser induced magnetization reversal in gdfeco nanostructures. Appl. Phys. Lett. *101*, 022410.

18. Mishra, K., Ciuciulkaite, A., Zapata-Herrera, M., Vavassori, P., Kapaklis, V., Rasing, T., Dmitriev, A., Kimel, A., and Kirilyuk, A. (2021). Ultrafast demagnetization in a ferrimagnet under electromagnetic field funneling. Nanoscale *13*, 19367–19375.

19. Mishra, K., Rowan-Robinson, R.M., Ciuciulkaite, A., Davies, C.S., Dmitriev, A., Kapaklis, V., Kimel, A.V., and Kirilyuk, A. (2022). Ultrafast demagnetization control in magnetophotonic surface crystals. Nano Lett. *22*, 9773–9780.

20. Beaurepaire, E., Merle, J., Daunois, A., and Bigot, J. (1996). Ultrafast spin dynamics in ferromagnetic nickel. Phys. Rev. Lett. *76*, 4250–4253.

21. Xu, Y., Deb, M., Malinowski, G., Hehn, M., Zhao, W., and Mangin, S. (2017). Ultrafast magnetization manipulation using single femtosecond light and hot-electron pulses. Adv. Mater. *29*, 1703474.

22. Banerjee, C., Teichert, N., Siewierska, K.E., Gercsi, Z., Atcheson, G.Y.P., Stamenov, P., Rode, K., Coey, J.M.D., and Besbas, J. (2020). Single pulse all-optical toggle switching of magnetization without gadolinium in the ferrimagnet mn2ruxga. Nat. Commun. *11*, 4444–4446.

23. Gorchon, J., Lambert, C.-H., Yang, Y., Pattabi, A., Wilson, R.B., Salahuddin, S., and Bokor, J. (2017). Single shot ultrafast all optical magnetization switching of ferromagnetic co/pt multilayers. Appl. Phys. Lett. *111*, 042401.

24. Iihama, S., Xu, Y., Deb, M., Malinowski, G., Hehn, M., Gorchon, J., Fullerton, E.E., and Mangin, S. (2018). Single-shot multi-level all-optical magnetization switching mediated by spin transport. Adv. Mater. *30*, 1804004.

25. Igarashi, J., Remy, Q., Iihama, S., Malinowski, G., Hehn, M., Gorchon, J., Hohlfeld, J., Fukami, S., Ohno, H., and Mangin, S. (2020). Engineering single-shot all-optical switching of ferromagnetic materials. Nano Lett. *20*, 8654–8660.

26. Vomir, M., Albrecht, M., and Bigot, J.-Y. (2017). Single shot all optical switching of intrinsic micron size magnetic domains of a pt/co/pt ferromagnetic stack. Appl. Phys. Lett. *111*, 242404.

27. Camsari, K.Y., Faria, R., Sutton, B.M., and Datta, S. (2017). Stochastic p-bits for invertible logic. Phys. Rev. X *7*, 031014.

28. Caravelli, F., and Nisoli, C. (2020). Logical gates embedding in artificial spin ice. New J. Phys. *22*, 103052.

29. Tanaka, G., Yamane, T., Héroux, J.B., Nakane, R., Kanazawa, N., Takeda, S., Numata, H., Nakano, D., and Hirose, A. (2019). Recent advances in physical reservoir computing: a review. Neural Netw. *115*, 100–123.

30. Marković, D., Mizrahi, A., Querlioz, D., and Grollier, J. (2020). Physics for neuromorphic computing. Nat. Rev. Phys. *2*, 499–510.

31. Gartside, J.C., Stenning, K.D., Vanstone, A., Holder, H.H., Arroo, D.M., Dion, T., Caravelli, F., Kurebayashi, H., and Branford, W.R. (2022). Reconfigurable training and reservoir computing in an artificial spin-vortex ice via spin-wave fingerprinting. Nat. Nanotechnol. *17*, 460–469.

32. Stenning, K.D., Gartside, J.C., Manneschi, L., Cheung, C.T.S., Chen, T., Vanstone, A., Love, J., Holder, H.H., Caravelli, F., Everschor-Sitte, K., et al. (2022). Adaptive programmable networks for in materia neuromorphic computing. Preprint at arXiv. https://doi.org/10.48550/arXiv.2211.06373.

33. Jensen, J.H., Folven, E., and Tufte, G. (2018). Computation in artificial spin ice. In Artificial Life Conference Proceedings (MIT Press), pp. 15–22.

34. Jensen, J.H., and Tufte, G. (2020). Reservoir computing in artificial spin ice. In Artificial Life Conference Proceedings (MIT Press), pp. 376–383.

35. Hon, K., Kuwabiraki, Y., Goto, M., Nakatani, R., Suzuki, Y., and Nomura, H. (2021). Numerical simulation of artificial spin ice for reservoir computing. Appl. Phys. Express *14*, 033001.

36. Lendinez, S., and Jungfleisch, M.B. (2020). Magnetization dynamics in artificial spin ice. J. Phys. Condens. Matter *32*, 013001.

37. Chumak, A.V., Serga, A.A., and Hillebrands, B. (2017). Magnonic crystals for data processing. J. Phys. D Appl. Phys. *50*, 244001.

38. Barman, A., Mondal, S., Sahoo, S., and De, A. (2020). Magnetization dynamics of nanoscale magnetic materials: a perspective. J. Appl. Phys. *128*, 170901.

39. Kaffash, M.T., Lendinez, S., and Jungfleisch, M.B. (2021). Nanomagnonics with artificial spin ice. Phys. Lett. *402*, 127364.

40. Gartside, J.C., Vanstone, A., Dion, T., Stenning, K.D., Arroo, D.M., Kurebayashi, H., and Branford, W.R. (2021). Reconfigurable magnonic mode-hybridisation and spectral control in a bicomponent artificial spin ice. Nat. Commun. *12*, 2488.

41. Stenning, K.D., Gartside, J.C., Dion, T., Vanstone, A., Arroo, D.M., and Branford, W.R. (2021). Magnonic bending, phase shifting and interferometry in a 2d reconfigurable nanodisk crystal. ACS Nano *15*, 674–685.

42. Gartside, J.C., Jung, S.G., Yoo, S.Y., Arroo, D.M., Vanstone, A., Dion, T., Stenning, K.D., and Branford, W.R. (2020). Current-controlled nanomagnetic writing for reconfigurable magnonic crystals. Commun. Phys. *3*, 219.

43. Dion, T., Gartside, J.C., Vanstone, A., Stenning, K.D., Arroo, D.M., Kurebayashi, H., and Branford, W.R. (2022). Observation and control of collective spin-wave mode hybridization in chevron arrays and in square, staircase, and brickwork artificial spin ices. Phys. Rev. Res. *4*, 013107.

44. Vanstone, A., Gartside, J.C., Stenning, K.D., Dion, T., Arroo, D.M., and Branford, W.R. (2022). Spectral fingerprinting: microstate readout via remanence ferromagnetic resonance in artificial spin ice. New J. Phys. *24*, 043017.

45. Gypens, P., Leo, N., Menniti, M., Vavassori, P., and Leliaert, J. (2022). Thermoplasmonic nanomagnetic logic gates. Phys. Rev. Appl. *18*, 024014.

46. Wang, Y.-L., Xiao, Z.-L., Snezhko, A., Xu, J., Ocola, L.E., Divan, R., Pearson, J.E., Crabtree, G.W., and Kwok, W.-K. (2016). Rewritable artificial magnetic charge ice. Science *352*, 962–966.

47. Gartside, J.C., Burn, D.M., Cohen, L.F., and Branford, W.R. (2016). A novel method for the injection and manipulation of magnetic charge states in nanostructures. Sci. Rep. *6*, 32864.

48. Gartside, J.C., Arroo, D.M., Burn, D.M., Bemmer, V.L., Moskalenko, A., Cohen, L.F., and Branford, W.R. (2018). Realization of ground state in artificial kagome spin ice via topological defect-driven magnetic writing. Nat. Nanotechnol. *13*, 53–58.

49. Wang, R.F., Nisoli, C., Freitas, R.S., Li, J., McConville, W., Cooley, B.J., Lund, M.S., Samarth, N., Leighton, C., Crespi, V.H., and Schiffer, P. (2006). Artificial 'spin ice'in a geometrically frustrated lattice of nanoscale ferromagnetic islands. Nature *439*, 303–306.

50. Skjærvø, S.H., Marrows, C.H., Stamps, R.L., and Heyderman, L.J. (2020). Advances in artificial spin ice. Nat. Rev. Phys. *2*, 13–28.

51. Zhang, W., Wang, Q., Zhao, C., and Song, Y. (2019). The optical cavity enhanced magneto-optical kerr effect signals of aao/al-based cofeb nanostructure arrays. Opt Commun. *437*, 44–49.

52. Zhang, W., Chen, Z., Belotelov, V.I., and Song, Y. (2022). Longitudinal magneto-optical kerr effect of nanoporous cofeb and w/cofeb/w thin films. Coatings *12*, 115.

53. Zhang, W., Wang, Y., Wang, Q., Belotelov, V.I., and Song, Y. (2018). The surface and interface engineering multilayered nanopore films for enhanced fabry–pérot interferences. J. Phys. Chem. C *122*, 29457–29463.

54. Shilina, P.V., Ignatyeva, D.O., Kapralov, P.O., Sekatskii, S.K., Nur-E-Alam, M., Vasiliev, M., Alameh, K., Achanta, V.G., Song, Y., Hamidi, S.M., et al. (2021). Nanophotonic structures with optical surface modes for tunable spin current generation. Nanoscale *13*, 5791–5799.

55. Xiao, J., Bauer, G.E.W., Uchida, K.-c., Saitoh, E., and Maekawa, S. (2010). Theory of magnon-driven spin seebeck effect. Phys. Rev. B *81*, 214418.

56. Islam, M.T., Wang, X.S., and Wang, X.R. (2019). Thermal gradient driven domain wall dynamics. J. Phys. Condens. Matter *31*, 455701.

57. Hofherr, M., Häuser, S., Dewhurst, J.K., Tengdin, P., Sakshath, S., Nembach, H.T., Weber, S.T., Shaw, J.M., Silva, T.J., Kapteyn, H.C., et al. (2020). Ultrafast optically induced spin transfer in ferromagnetic alloys. Sci. Adv. *6*, eaay8717.

58. Dewhurst, J.K., Elliott, P., Shallcross, S., Gross, E.K.U., and Sharma, S. (2018). Laser-induced intersite spin transfer. Nano Lett. *18*, 1842–1848.

59. Willems, F., von Korff Schmising, C., Strüber, C., Schick, D., Engel, D.W., Dewhurst, J.K., Elliott, P., Sharma, S., and Eisebitt, S. (2020). Optical inter-site spin transfer probed by energy and spin-resolved transient absorption spectroscopy. Nat. Commun. *11*, 871.

60. Uba, S., Uba, L., Yaresko, A., Perlov, A.Y., Antonov, V., and Gontarz, R. (1996). Optical and magneto-optical properties of co/pt multilayers. Phys. Rev. B Condens. Matter *53*, 6526–6535.